PNAS
www.pnas.org

Supplementary Information for

Microfluidic protein isolation and sample preparation for high-resolution cryo-EM

Claudio Schmidli, Stefan Albiez, Luca Rima, Ricardo Righetto, Inayatulla Mohammed, Paolo Oliva, Lubomir Kovacik, Henning Stahlberg and Thomas Braun

Corresponding Author Name.
E-mail: thomas.braun@unibas.ch

This PDF file includes:

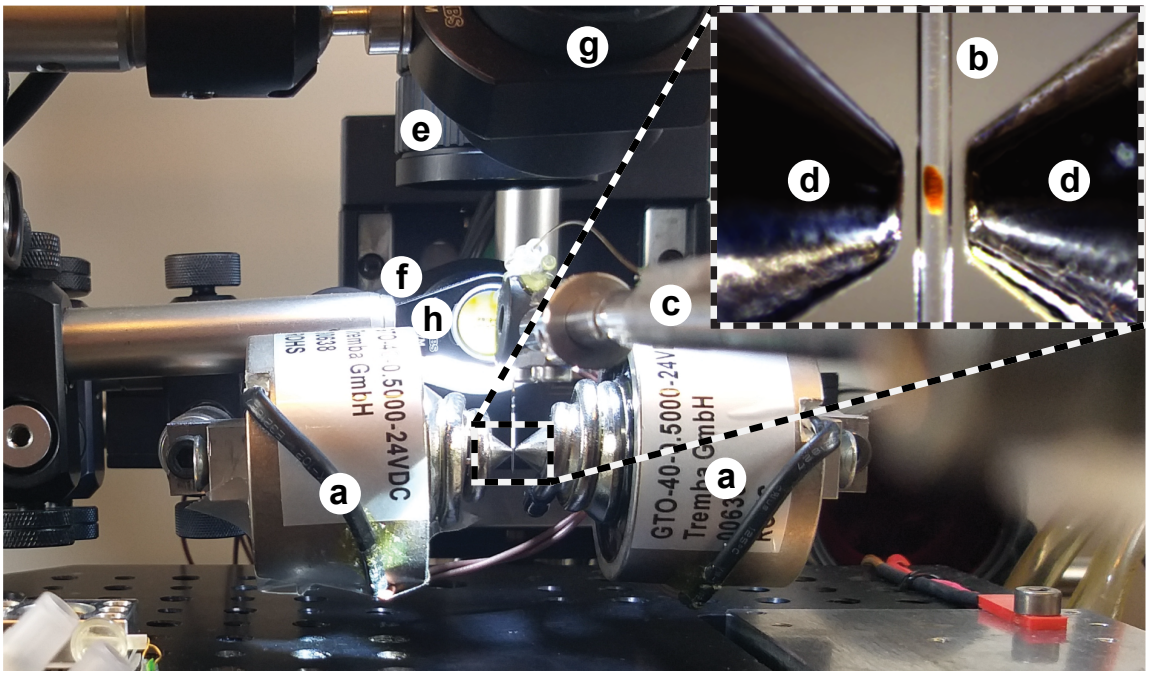

Fig. S1. Image of the magnetic trap set-up. The opposite poles of two 4.8 W electromagnets **(a)** are facing one another. A microcapillary **(b)**, held with the manipulator arm **(c)**, is placed between the two iron tips **(d)** of the electromagnets. The trapped magnetic plug can be observed with a camera **(e)** via a mirror **(f)**. The photo-cleavable cross-linker can be exposed to UV light using a LED **(g)** emitting light at 365 nm that is deflected by a mirror **(h)**.

Supporting Information Text

A. Characteristics of the magnetic trap. The magnetic particle trap consists of two electromagnets arranged with opposite poles facing one another (Fig. S1). Attached iron tips extend the magnet cores. This concentrates the magnetic flux to a small area and forms a strong field gradient between the two tips (see Fig. S2). For magnetic particle trapping, the front part of the microcapillary segment just above the nozzle was placed in this region using a motorized XYZ linear translation stage, and the sample was aspirated. The magnetic force acting on the super-paramagnetic particles immobilized the beads.

In experiments, super-paramagnetic beads with sizes from 15 nm to 1000 nm can be trapped and experience a magnetic force F_m acting on a saturated particle according to:

$$F_m = V \cdot M_S \cdot \mu_0 \cdot \nabla H \qquad [1]$$

where V is the volume of the magnetic particles, M_S the saturation magnetization, μ_0 the magnetic constant, and H the magnetic field strength. The current controls the field applied by the electromagnets. Due to the dependence on the volume (V), higher currents are needed in order to trap smaller particles. When the electromagnets are operated at maximum power, the core and the tips significantly heat up. For this reason, a cooling water system was implemented allowing the tips to be cooled to 4 °C by pumping water through a copper tubing twisted around them. Both, the copper tubing and the iron tips were coated with nickel to reduce corrosion. The magnetic trap is mounted on a motorized stage, allowing it to be moved in the vertical direction, independent of the microcapillary manipulator arm. For sample uptake, the magnetic trap and microcapillary were simultaneously moved down to insert the nozzle tip of the capillary into the sample well.

The parts used to build the magnetic trap are summarized in Table S1. Connecting parts were manufactured by the workshop of the Biozentrum, University of Basel, Switzerland. Plans are available upon request. Further cryoWriter parts used for grid preparation are described in (1).

Fig. S2 shows a finite element simulation of the magnetic flux density within the magnetic trap system, which was caluclated with COMSOL Multiphysics. Soft-iron material properties were applied to the magnet cores and tips using a non-linear B-H curve that includes saturation effects. The windings were modelled with coil features.

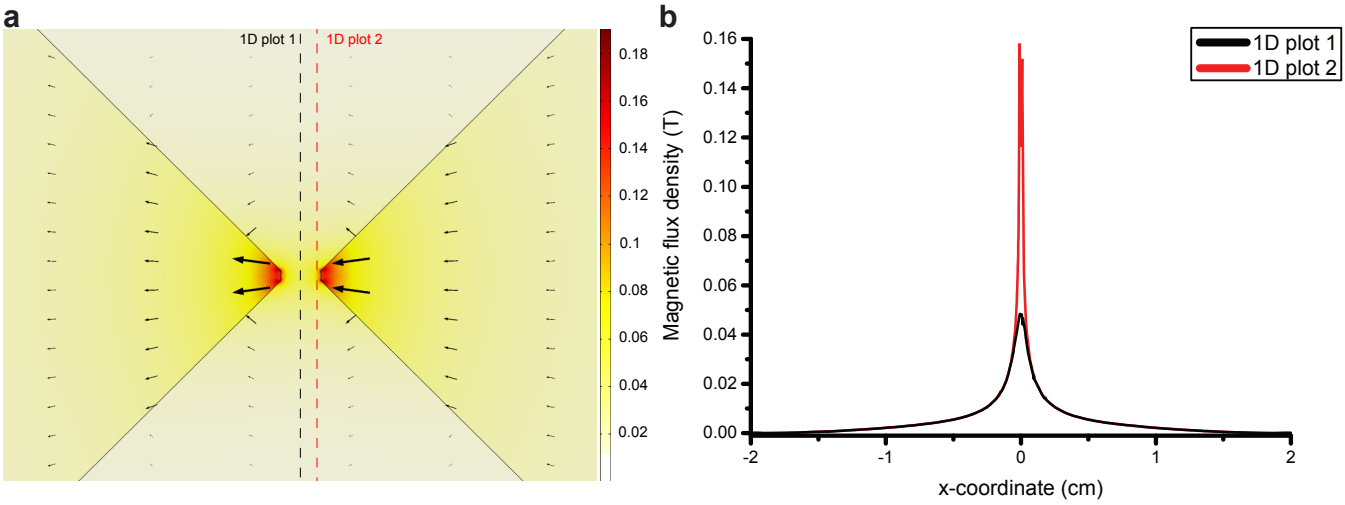

Fig. S2. Finite element simulation of the magnetic field generated by the electromagnetic trap system. **(a)** 2D plot of the magnetic flux density around the iron tips (black solid lines). The direction of the magnetic fields is shown with black arrows. The size of the arrows is proportional to the field strength. The values in the color scale are given in Tesla (T). **(b)** Extracted 1D plots of the magnetic flux density from the 2D plot in (a) at the positions indicated with dashed lines. The figure shows that between the tips (x=0) the highest field gradients are observed. This leads to a magnetic force F_m pushing magnetic particles towards this region.

Part Name	Part Number	Distributor
Electromagnet	GTO-40-0.5000-24VDC	Conrad Electronic AG
Iron magnet tips with copper cooling tubes	-	In-house production
Cooling pump	2449120	Digitec Galaxus AG
Tubing for cooling system	1025U04	Parker Hannifin
Tubing for cooling system	1025U06	Parker Hannifin
Motorized stage for vertical trap movement	M-126.PD2	Dyneos AG
Connector plate (trap-stage)	-	In-house production
Camera (Magnetic Trap)	NetFOculusFO124TC	NET GmbH
Optics (for magnetic trap camera)	MLM3X-MP	FRAMOS GmbH
Mirror (for magnetic trap camera)	PF07-03-P01	Thorlabs
UV LED	M365LP1c	Thorlabs
Dielectric Mirror (to deflect UV beam)	BB0511-E01	Thorlabs
Syringe pump controller	A3921000093	Cetoni
Syringe pump dosing unit	A3921000095	Cetoni
Liquid handling syringe	HA-80901	BGB Analytik AG
Microcapillary tubing	TSP-150375-D-10	BGB Analytik AG
Liquid handling nozzle	FS360-150-30-N-5-C12	MS Wil GmbH
PressFit Connector (nozzle-microcapillary)	2525LD	BGB Analytik AG

Table S1. Parts list of the magnetic trap setup.

B. Enclosure of sample between air bubbles. The sample can optionally be enclosed between air bubbles that are separated by washing buffer. The air bubbles act as barriers for the protein particles and reduce dilution by diffusion and Taylor dispersion. In this experiment two 6 nL air bubbles separated by 25 nL washing buffer containing 1 mg TMV were used (Fig. S3).

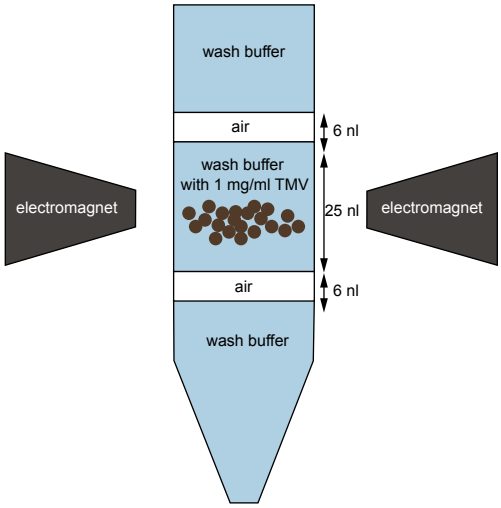

Fig. S3. Illustration of the magnetic particle-plug enclosed between two 6 nL air bubbles for UV exposure and elution. The air bubbles act as barriers preventing diffusion and Taylor dispersion to keep the protein concentration as high as possible.

C. Data collection and image processing parameters. The data collection parameters are provided in Table S2, and the main image processing parameter used for the 20S proteasome and TMV are given in Tables S3 & S4.

Data collection	
Voltage	300 kV
Physical pixel size	0.812 Å
Super-resolution pixel size	0.406 Å
GIF zero loss energy window	20 eV
Defocus range	−1.0 µm to −2.2 µm
K2 operating mode	8k super-resolution (with electron counting)
Number of frames	30
Second per frame	0.2
Total dose	72 $e^-/Å^2$
Number of micrographs	523

Table S2. Data collection parameters.

Image processing 20S proteasome	
Micrographs	523
Box size	480 pixel
Box size (after down-sampling)	384 pixel
Pixel size (after down-sampling)	1.015 Å
Gautomatch picked particles	55,135
Particles after 2D classification	38,848
Particles for 3D refinement	16,015
Symmetry	C2
Final resolution	3.5 Å
Estimated map sharpening B-factor	−39.2 $Å^2$

Table S3. Image processing parameters used for 20S proteasome structure determination with RELION3.

Image processing TMV	
Micrographs	481
Box size	420 pixel
Number of asymetric units	31
Picked end-to-end coordinated	2,676
Extracted particles	52,806
Helical twist	22.03°
Helical rise	1.41 Å
Local searches of symmetry	No
Particles after 2D classification	52,806
Particles after 3D refinement	52,776
Symmetry	C1
Final resolution	1.9 Å
Estimated map sharpening B-factor	−38.9 $Å^2$

Table S4. Image processing parameters used for helical structure determination of TMV with RELION3.

D. Fourier shell correlation and local resolution histograms. We used the Fourier shell correlation method (2) between two independently refined half-maps ('gold standard') (3) to estimate the resolution of our 3D reconstructions (Fig. S4a). A threshold of 0.143 on the FSC curve was adopted to define the resolution limit of the reconstruction (4). The FSC curves were corrected for artificial correlations introduced by masking (5). We found a global resolution of 3.5 Å for the 20S proteasome and of 1.9 Å for the TMV. These estimates correlate well with the features observed in the maps (see Fig. 3 of the main text for the 20S proteasome and chapter G for the TMV). The estimated resolution is further corroborated by the local resolution histograms shown in Fig. S4b, which display the normalized counts of voxels at each resolution. The resolution for the proteasome varies significantly; for more details, see Chapter E. The local resolution was assessed based on the half-maps using the method described in (6), as implemented in RELION3, with a map sampling of 25 Å (Fig. S4b).

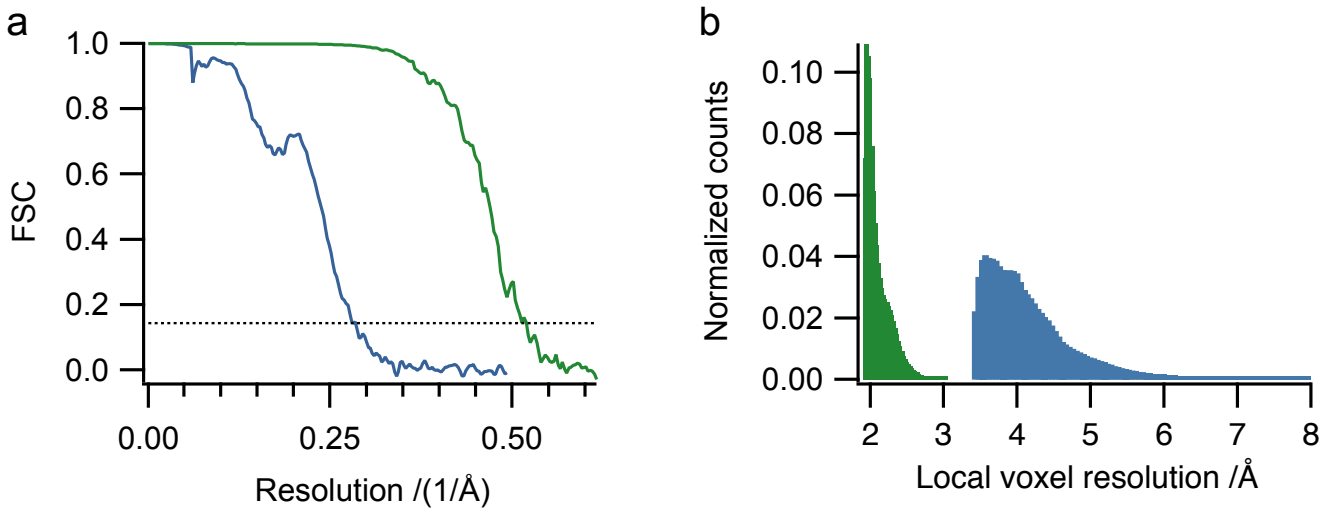

Fig. S4. Resolution estimation for the 20S proteasome (blue) and TMV (green). (**a**) Fourier shell correlation from the RELION3 refinement. (**b**) Histograms depicting the normalized voxel counts per resolution range.

E. Local resolution map of the 20S proteasome. Fig. S5 shows the local resolution calculated for the 20S proteasome using RELION3. Note that the active domains (indicated by red arrowheads in Fig. S5) are less well resolved than the other domains, and are associated with the catalytic subunits of the β-ring. Interestingly, the resolution of the α-ring around the pseudo-seven-fold axis is quite heterogeneous, whereas the β-ring exhibits lower resolution around subunits $\beta 4$ and $\beta 5$. Since subunits $\beta 4$, $\beta 5$ and $\beta 6$ are the catalytically active elements (7), the lower resolution of subunits $\beta 4$ and $\beta 5$ suggests that these are trapped in various conformations during cryo-EM grid preparation.

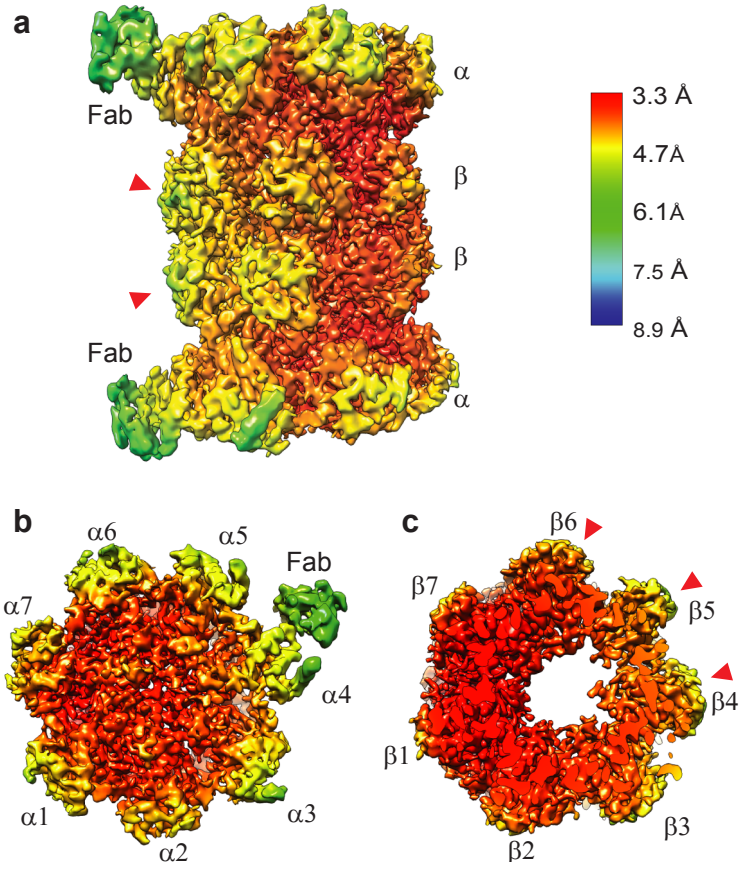

Fig. S5. Local resolution map for the human 20S proteasome at a global resolution of 3.5 Å. (**a**) Side view with annotated Fabs. (**b**) Local resolution of the α-subunits. (**c**) Local resolution of the β-subunits. The red arrowheads indicate the catalytically active subunits.

F. Model building results. After initial rigid body fitting, the 20S proteasome and TMV models were refined using PHENIX. The models were assessed by the fit to the experimental density and validated with clashscore, Ramachandran statistics, and good bond/angle lengths as shown in Tables S5 & S6. Additionally, a random shift (mean 0.3 Å) was introduced to the final models and each model was refined with the same settings against one unfiltered half map (half-map 1). The FSC curves of the models against half-map 1 and the other half map (half-map 2) was then calculated (Fig. S6 & S7). The fact the both curves look very similar indicates that no overfitting took place.

Phenix Real-Space Refinement	
Map CC (around atoms)	0.80

MolProbity(8)	
All-atom clashscore	4.79
Ramachandran favored	96 %
Ramachandran allowed	2.43 %
Ramachandran outliers	0.26 %
Rotamer outliers	0.52 %
Cb deviations	0
RMSD (bonds)	0.008
RMSD (angles)	1.044

Table S5. 20S proteasome model validation statistics.

Phenix Real-Space Refinement	
Map CC (around atoms)	0.87

MolProbity(8)	
All-atom clashscore	0.84
Ramachandran favored	97.35 %
Ramachandran allowed	2.65 %
Ramachandran outliers	0 %
Rotamer outliers	0 %
Cb deviations	0
RMSD (bonds)	0.006
RMSD (angles)	0.932

Table S6. TMV model validation statistics.

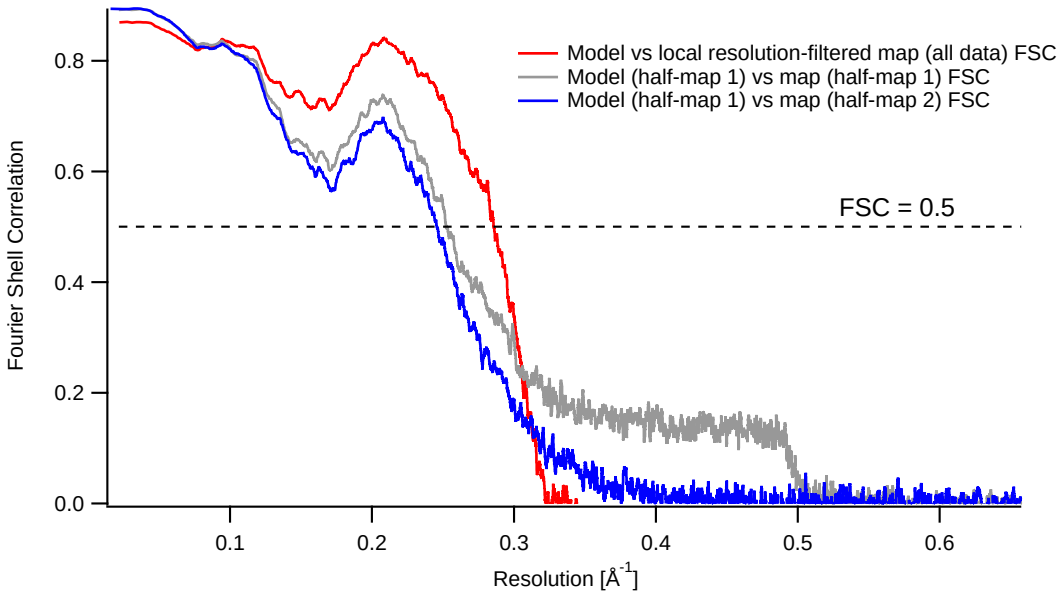

Fig. S6. FSC curve of the final 20S proteasome model versus the full map (all data), against which the model was refined (red). The full map used to calculate the FSC was resolution filtered. FSC curve of the final 20S proteasome model with randomized coordinates shifts (mean shifts of 0.3 Å) versus the first unfiltered half-map (half-map 1) against which it was refined (grey) and versus the second half-map (half-map 2) against which it was not refined (blue).

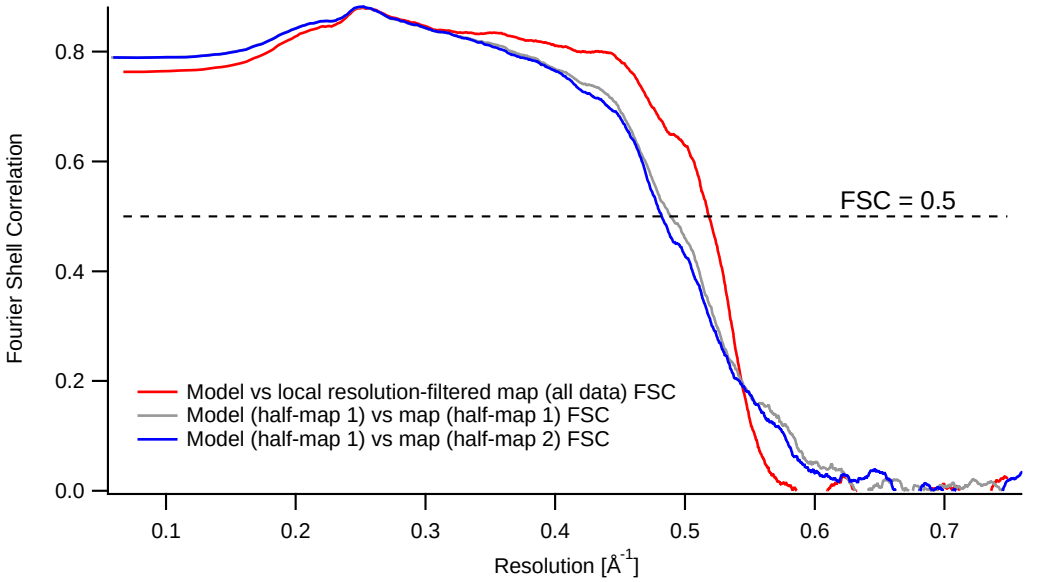

Fig. S7. FSC curve of the final TMV model versus the full map (all data), against which the model was refined (red). The full map used to calculate the FSC was resolution filtered. FSC curve of the final TMV model with randomized coordinates shifts (mean shifts of 0.3 Å) versus the first unfiltered half-map (half-map 1) against which it was refined (grey) and versus the second half-map (half-map 2) against which it was not refined (blue).

G. Three-dimensional map of TMV. Fig. S8 demonstrates the high quality of the microfluidic grid preparation. We report here the map of TMV at a global resolution of 1.9 Å. Compared to the 20S proteasome, this map has both higher global resolution (see FSC curve in D, Fig. S4a) and less variable local resolution (Fig. S4b) due to the higher rigidity of the structure and the helical symmetry averaging imposed on the reconstruction.

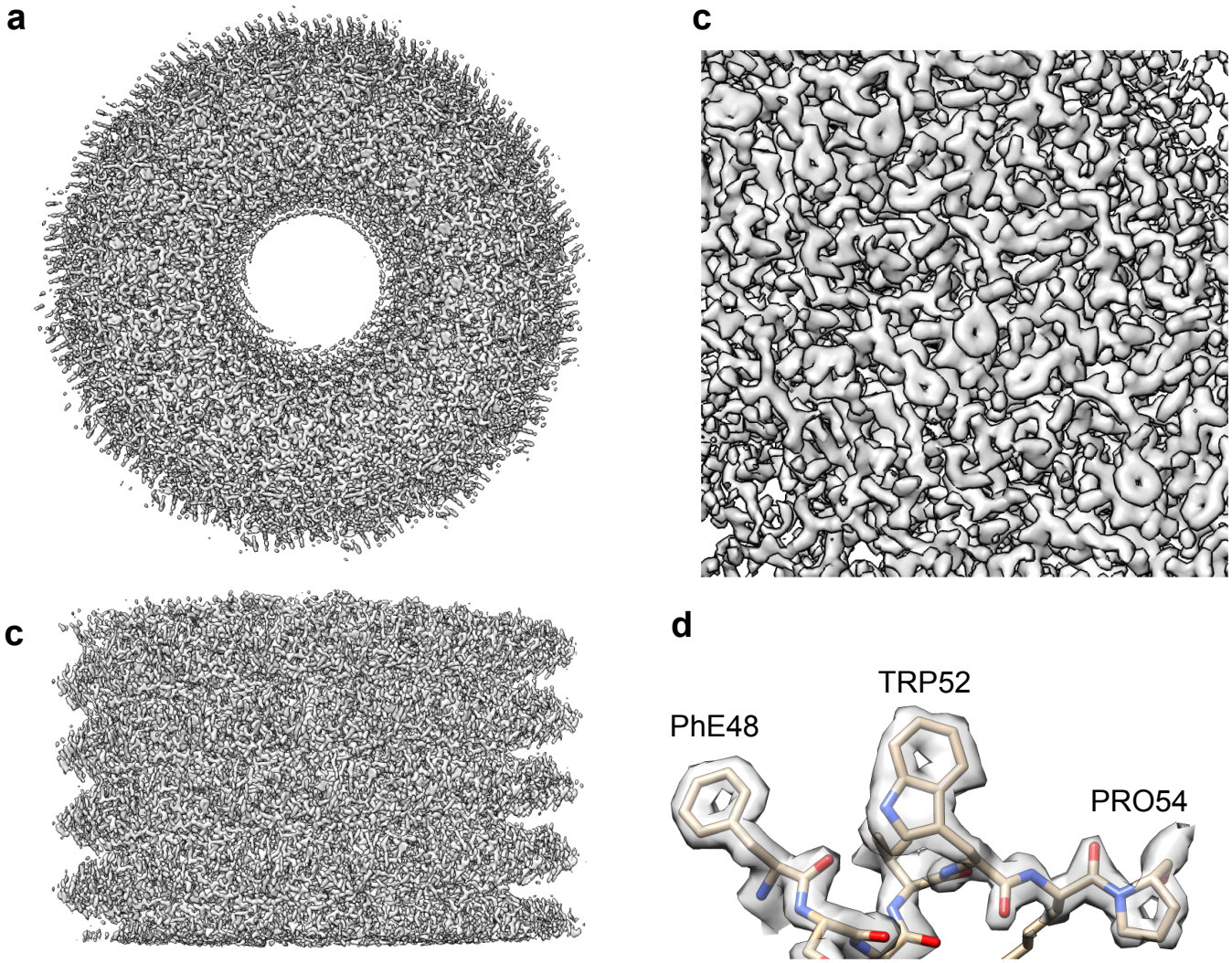

Fig. S8. 3D reconstruction of TMV at a global resolution of 1.9 Å showing the top view (**a**) and the side view (**b**) of the electron density map. The zoom-in (**c**) demonstrates the high resolution features of the map. At this resolution it is possible to see the holes of the aromatic rings (**d**).

References

1. Claudio Schmidli, Luca Rima, Stefan A Arnold, Thomas Stohler, Anastasia Syntychaki, Andrej Bieri, Stefan Albiez, Kenneth N Goldie, Mohamed Chami, Henning Stahlberg, and Thomas Braun. Miniaturized sample preparation for transmission electron microscopy. *JoVE*, (137):e57310, 2018. .
2. George Harauz and Marin van Heel. Exact filters for general geometry three dimensional reconstruction. *Optik*, 78(4):146–156, 1986. ISSN 0030-4026. URL http://md1.csa.com/partners/viewrecord.php?requester=gs{&}collection=TRD{&}recid=1507969EA.
3. Sjors H.W. W Scheres and Shaoxia Chen. Prevention of overfitting in cryo-Em structure determination. *Nat. Methods*, 9(9): 853–854, jul 2012. ISSN 15487091. . URL http://dx.doi.org/10.1038/nmeth.2115.
4. Peter B Rosenthal and Richard Henderson. Optimal determination of particle orientation, absolute hand, and contrast loss in single-particle electron cryomicroscopy. *J. Mol. Biol.*, 333(4):721–745, oct 2003. ISSN 0022-2836. . URL http://www.sciencedirect.com/science/article/pii/S0022283603010222.
5. Shaoxia Chen, Greg McMullan, Abdul R. Faruqi, Garib N. Murshudov, Judith M. Short, Sjors H.W. W Scheres, and Richard Henderson. High-resolution noise substitution to measure overfitting and validate resolution in 3D structure determination by single particle electron cryomicroscopy. *Ultramicroscopy*, 135(0):24–35, dec 2013. ISSN 0304-3991. . URL http://dx.doi.org/10.1016/j.ultramic.2013.06.004http://www.sciencedirect.com/science/article/pii/S0304399113001472.
6. Giovanni Cardone, J Bernard Heymann, and Alasdair C Steven. One number does not fit all: Mapping local variations in resolution in cryo-EM reconstructions. *J. Struct.l Biol.*, 184(2):226–236, 2013. ISSN 1047-8477. .
7. Paula C. A. da Fonseca and Edward P. Morris. Cryo-EM reveals the conformation of a substrate analogue in the human 20S proteasome core. *Nat. Commun.*, 6(7573), July 2015. ISSN 2041-1723. .
8. Andrew Leaver-Fay, Gary J. Kapral, Ian W. Davis, Jack Snoeyink, Jane S. Richardson, Jeremy N. Block, Laura W. Murray, Vincent B. Chen, III Arendall, W. Bryan, Xueyi Wang, and David C. Richardson. MolProbity: all-atom contacts and structure validation for proteins and nucleic acids. *Nucleic Acids Research*, 35(suppl_2):W375–W383, 07 2007. ISSN 0305-1048. . URL https://dx.doi.org/10.1093/nar/gkm216.